Influence of the Heating Protocol on the Crystallographic Texture and Electrical Properties of CuO Layers Formed by Thermal Oxidation of Cu

Germán ESCALANTE-NOTARIO [1], Roberto LÓPEZ [2 *], Antonio COYOPOL [3], Román ROMANO-TRUJILLO [3], Sergio JIMÉNEZ-SANDOVAL [4]

[1] *Universidad Autónoma de Campeche, Posgrado de la Facultad de Ingeniería, Campus V, Col. Ex-Hacienda Kalá, San Francisco de Campeche, 24085, México*
[2] *TECNM / Tecnológico de Estudios Superiores de Jocotitlán, Carretera Toluca-Atlacomulco km 44.8, Jocotitlán, Estado de México, 50700, México*
[3] *Centro de Investigaciones en Dispositivos Semiconductores, Instituto de Ciencias, BUAP, 14 Sur y Av. San Claudio, C.U., Edificio IC-6, Puebla, 72570, México*
[4] *Unidad Querétaro, Centro de Investigación y de Estudios Avanzados del IPN, Querétaro, 76230, Mexico*

http://doi.org//10.5755/j02.ms.44611

Received 23 March 2026; accepted 30 April 2026

CuO layers were formed by thermal oxidation of Cu sheets at 900 °C under static-air conditions using two different heating protocols: isothermal insertion into a preheated furnace and continuous ramp heating from room temperature. X-ray diffraction analysis revealed predominantly monoclinic CuO in both cases. The isothermal insertion protocol produced a distributed preferential orientation involving the (111), (020), and (311) planes, whereas the continuous ramp protocol promoted a pronounced texture along the (−202) plane, accompanied by larger crystallite size and reduced microstrain. Minor Cu_2O traces were detected in samples prepared under the continuous ramp protocol, indicating differences in oxidation kinetics. Raman peak positions were nearly identical (< 1.5 cm^{-1} variation), indicating similar local bonding in both samples, while slightly broader full width at half maximum (FWHM) values for the isothermal insertion sample were consistent with the higher microstrain derived from XRD analysis. Photoluminescence measurements showed emission maxima at ~880 nm for the continuous ramp sample and ~887 nm for the isothermal insertion sample, with nearly identical FWHM values (~ 153 – 154 nm). The red shift observed for the isothermal insertion sample suggests minor variations in the local defect environment, while the comparable FWHM values indicate that the same dominant defect-related recombination mechanism governs the emission in both cases. Electrical transport properties were largely insensitive to the texture and microstructural variations induced by the heating protocol. The heating protocol therefore exerts a clear influence on the crystallographic texture of CuO layers formed by thermal oxidation of Cu, without significantly altering their electrical behavior.

Keywords: CuO layers, thermal oxidation of copper, heating protocol, crystallographic texture, Raman spectroscopy, Hall effect.

1. INTRODUCTION

CuO is a p-type semiconductor with a narrow band gap in the range of 1.3 – 2.1 eV, arising mainly from intrinsic point defects such as oxygen vacancies and interstitial oxygen [1, 2]. Owing to its favorable electrical and optical properties, CuO has attracted considerable interest for applications in electronic devices [3], gas sensors [4], and energy-related technologies [5]. In these applications, the carrier concentration, mobility, and electrical conductivity of CuO are strongly influenced by its microstructure and defect density, which are, in turn, determined by the synthesis and processing conditions. A wide variety of techniques have been employed for the fabrication of CuO layers, including pulsed laser deposition [6], sputtering [7], atomic layer deposition [8], and molecular beam epitaxy [9]. While these methods allow precise control over film thickness and composition, they often require sophisticated equipment and vacuum environments. In contrast, thermal oxidation of metallic Cu in a furnace represents a simple, cost-effective, and scalable route for producing CuO layers, making it particularly attractive for large-area and industrial applications. Previous studies have demonstrated that parameters such as oxidation temperature, oxidation time, and post-deposition thermal treatments play a crucial role in determining the structural and electrical properties of CuO. For instance, sputtered CuO-based diodes subjected to different annealing conditions exhibited Schottky barrier heights ranging from 0.84 to 1.12 eV, highlighting the strong sensitivity of the electronic properties of CuO to the thermal history [10]. While the effects of temperature, time, and annealing conditions have been previously investigated, the role of the heating protocol itself, specifically whether the Cu substrate is heated gradually from room temperature or inserted directly into a preheated furnace, has received limited attention. In thermally oxidized Cu systems, the heating protocol may influence crystallographic texture and defect formation through its effect on oxidation kinetics and oxygen diffusion, particularly because intermediate oxide phases such as Cu_2O can form at lower temperatures before

* Corresponding author: R. López
E-mail: *roberto.lopez@tesjo.edu.mx*

transforming into CuO [11 – 13]. The comparison between continuous ramp heating and isothermal insertion is therefore relevant, as these approaches impose different thermal histories. During gradual heating, the Cu substrate remains within intermediate temperature ranges where Cu_2O formation is favored, potentially affecting the subsequent transformation into CuO and the microstructure. In contrast, direct insertion into a preheated furnace imposes a rapid transition to high temperature, altering oxidation kinetics and limiting the formation of intermediate oxide phases. This may lead to differences in crystallographic texture, crystallite size, and defect-related properties.

In this work, CuO layers were grown by thermal oxidation of Cu sheets under different heating protocol. Structural properties were analyzed by X-ray diffraction to determine phase composition, crystallographic texture, crystallite size, microstrain, and dislocation density. Raman spectroscopy and photoluminescence measurements were employed to probe local lattice distortions and defect-related states, while Hall effect measurements were performed to evaluate charge transport properties and their relation to the microstructural characteristics.

2. EXPERIMENTAL DETAILS

CuO layers were grown by thermal oxidation of metallic Cu sheets. Commercial Cu sheets with an area of 1 cm^2 and a thickness of 500 μm were used as substrates. Prior to oxidation, the Cu sheets were cleaned to remove surface contaminants and grease by sequential ultrasonic cleaning in acetone and ethanol for 5 min each, followed by drying in air. Thermal oxidation was performed in a horizontal tube furnace (CMOD-HAT-1100D25) under static-air conditions at a fixed temperature of 900 °C for 8 h. Two different heating protocols were employed. In the continuous ramp protocol, the Cu sheets were placed inside the furnace at room temperature, and the temperature was then increased up to 900 °C at the furnace's programmed heating rate. In the isothermal insertion protocol, the furnace was first heated to 900 °C, and the Cu sheets were subsequently inserted into the hot zone once the temperature was stabilized. In both cases, after completion of the oxidation treatment, the samples were allowed to cool naturally to room temperature inside the furnace. X-ray diffraction (XRD) measurements were carried out at room temperature using a Bruker D8 Discover diffractometer with Cu Kα radiation (λ = 1.5406 Å). Diffraction patterns were recorded over the 2θ range of 25 – 75°, using 3001 data points with a step time of 1 s per point. Phase identification was performed by comparison with the powder diffraction file (PDF) database. Crystallographic texture was evaluated through the calculation of the texture coefficient using normalized peak intensities. The crystallite size, microstrain, and dislocation density were estimated from the full width at half maximum of the diffraction peaks using the Scherrer equation and standard relations reported in the literature. For Raman spectroscopy measurements, the 633 nm wavelength of a He–Ne laser was employed as the excitation source in a Raman Horiba Jobin-Yvon system. Photoluminescence (PL) spectra were acquired using the same optical setup under identical excitation conditions by recording the emitted signal as a function of wavelength. Electrical properties were determined by Hall effect measurements performed at room temperature (298 K) using an ECOPIA HMS-5000 Hall effect measurement system configured in the van der Pauw geometry. Ohmic contacts were formed by soldering indium at the four corners of the samples. A constant current of 10 mA was applied, and a magnetic field of 0.55 T was used during the measurements. The positive sign of the Hall coefficient indicated that the type of conductivity.

3. RESULTS AND DISCUSSION

The structural properties of the thermally oxidized CuO layers were first examined by X-ray diffraction (XRD). Figure 1a shows the XRD diffractogram of the CuO layer obtained using the isothermal insertion heating protocol. The diffraction peaks located at 2θ = 32.31, 35.32, 38.54, 53.26, 65.68, 67.91, and 72.26° correspond to the (−110), (002), (111), (020), (022), (113), and (311) crystallographic planes of monoclinic CuO (PDF 00-045-0937), respectively. The experimental peak positions match the reference values within ± 0.3°, confirming that the sample predominantly consists of the CuO phase, with no detectable contributions from secondary phases such as Cu_2O or metallic Cu. The presence of sharp and well-defined diffraction peaks indicates a high degree of crystallinity. The relatively high intensity of the reflection at $2\theta \approx 38.54°$, associated with the (111) plane, suggests the possible existence of a preferred orientation. To quantify the degree of crystallographic texture, the texture coefficient (TC) was calculated using Eq. 1 [14].

$$TC(h_i k_i l_i) = \frac{I(h_i k_i l_i)}{I_o(h_i k_i l_i)} \left\{ \frac{1}{n} \sum_{i=1}^{n} \frac{I(h_i k_i l_i)}{I_o(h_i k_i l_i)} \right\}^{-1}, \quad (1)$$

where *I(hkl)* is the experimental intensity of the diffraction peak corresponding to the *(hkl)* plane; I_o*(hkl)* is the standard intensity reported in the powder diffraction file database, and *n* is the total number of planes considered. The TC was calculated using CuO diffraction peaks detected in each sample, considering only reflections with sufficient intensity for reliable analysis. Both the experimental intensities and the standard reference values from PDF 00-045-0937 were normalized with respect to the sum of the selected peaks. A TC = 1 corresponds to a randomly oriented polycrystalline material, whereas TC > 1 indicate preferred orientation along the corresponding crystallographic direction, while values less than 1 suggest under-representation compared to a randomly oriented standard. The TC values calculated for the isothermal insertion protocol are shown in Fig. 1 b. The (111), (020), and (311) planes exhibit TC values greater than unity, indicating that these orientations were favored during CuO growth. Notably, although the (111) reflection shows a high absolute intensity, the (311) plane exhibits the highest TC value (≈ 1.89), demonstrating that peak intensity alone is not sufficient to accurately assess a preferred orientation. Structural parameters, including crystallite size (*D*), microstrain (ε), and dislocation density (δ), were estimated to evaluate lattice imperfections in the CuO layers [15]. The crystallite size was estimated by the Scherrer equation:

$$D = \frac{k\lambda}{\beta \cos\theta}, \quad (2)$$

where D is measured in nm; K is the shape constant (0.9); λ is the CuK radiation (0.15406 nm); β is the full width at half maximum (in radians); θ is the diffraction angle (in radians).

The β was of 0.15 ° (0.003645 rad) for the isothermal insertion protocol sample. The micro-strain was calculated using the relation:

$$\varepsilon = \frac{\beta}{4\,tan\theta}. \quad (3)$$

The dislocation density was determined using the formula:

$$\delta = \frac{n}{D^2}, \quad (4)$$

where n is a factor, which gives the minimum dislocation density when is equal to unity. The D was then of an average value of 56.11 nm for the isothermal insertion protocol. The corresponding ε and δ were of 18.7×10^{-4} and 3.18×10^{-4} nm^{-2}, respectively (Table 1). Fig. 1 c shows the XRD diffractogram of the CuO layer obtained using the continuous ramp heating protocol. Diffraction peaks located at 2θ = 32.18, 35.21, 38.46, 48.48, 58.03, 61.16, 65.68, 66.06, 67.77, and 72.26° correspond to the (−110), (002), (111), (−202), (202), (−113), (022), (−311), (113), and (311) planes of monoclinic CuO, respectively. In addition to these reflections, a weak peak observed at $2\theta \approx 73.27°$ is assigned to the (311) plane of Cu_2O (PDF 00-005-0667), indicating incomplete oxidation of Cu under the continuous ramp protocol. Although both samples were oxidized at 900 °C for the same duration, the appearance of the Cu_2O phase in the continuous ramp sample suggests that the thermal path followed during heating plays a role in phase evolution. During gradual heating from room temperature, Cu passes through a temperature range (~ 200 – 500 °C), where Cu_2O formation is thermodynamically favored. The subsequent transformation to CuO at higher temperatures may be kinetically hindered by the Cu_2O layer that limits oxygen diffusion [16]. The TC values corresponding to the continuous ramp protocol are shown in Fig. 1 d. While the (202) plane exhibits a TC value close to unity (≈ 1.12), the (−202) plane shows a markedly higher TC value of 4.17, indicating a strong preferential orientation along this direction. In contrast, the (002) plane (typically the most intense reflection in the standard CuO powder pattern), shows a significantly reduced TC value (≈ 0.12), indicating suppression of this orientation. The occurrence of preferred orientation in CuO layers has been previously reported and is known to be highly sensitive to the growth conditions. For instance, some workers have shown that the preferred orientation in sputtered CuO layers can be adjusted by varying the oxygen flow rate, where low oxygen flow rates promote a (111) preferred orientation, whereas higher flow rates favor the development of a (−111) texture [17]. Additionally, other workers indicate that CuO layers deposited by spray pyrolysis predominantly exhibit a (−111) orientation [18]. In this context, the preferential orientations observed in the present thermally oxidized CuO layers suggest that the heating protocol plays a role analogous to other process parameters (such as oxygen partial pressure), in determining the crystallographic texture. Specifically, the isothermal insertion protocol yields moderate TC values (>1) distributed among the (111), (020), and (311) planes, indicating a mixed but non-random texture, whereas the continuous ramp protocol produces a markedly stronger and more localized preferential orientation along the (−202) plane, with a TC value of 4.17, accompanied by the suppression of the (002) orientation.

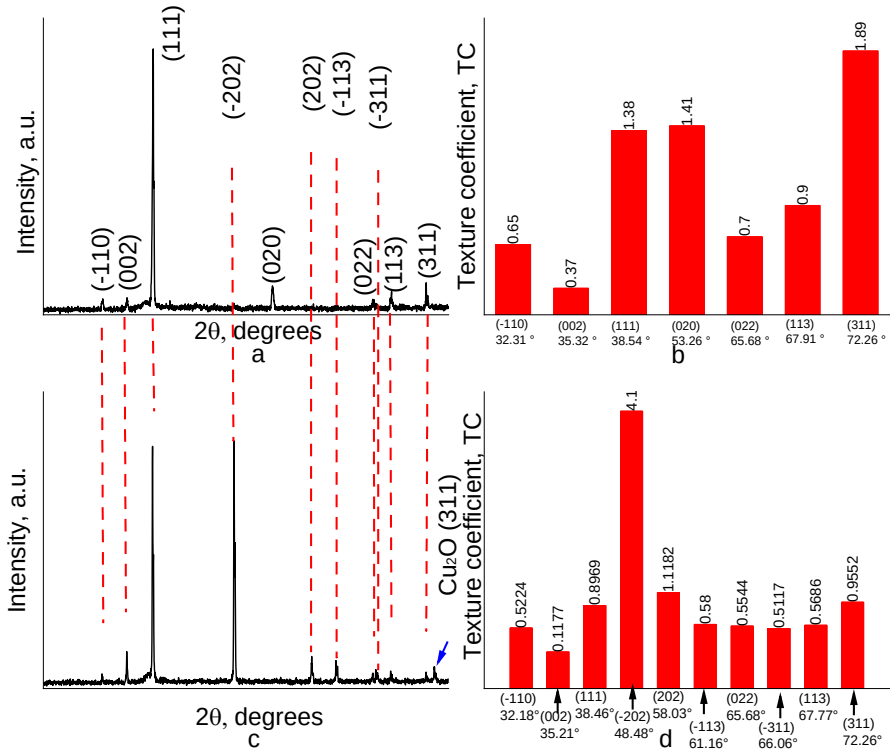

Fig. 1. XRD diffractograms and TC of the CuO layers: a, b – for isothermal insertion; c, d – for continuous ramp

Table 1. Crystallite size, micro-strain and dislocation density of the CuO layers obtained by thermal oxidation of Cu in two different heating protocols

Heating protocol	D, nm	$\varepsilon x10^{-4}$	$\delta \times 10^{-4}$, nm^{-2}
Isothermal insertion	56.11	18.7	3.18
Continuous ramp	79.20	10.7	1.59

These results demonstrate that, even under identical oxidation temperature and time, variations in the heating protocol can lead to substantial differences in the crystallographic texture. The structural parameters derived for the continuous ramp sample are summarized in Table 1. Compared to the isothermal insertion protocol, the continuous ramp protocol results in a larger crystallite size (79.20 nm) as well as lower microstrain (10.7×10^{-4}) and dislocation density (1.59×10^{-4} nm^{-2}), indicating improved structural order and enhanced grain growth. However, despite the apparent improvement in crystalline quality, the presence of the Cu_2O diffraction peak suggests that the continuous ramp protocol may be less effective in achieving complete oxidation of Cu under the conditions investigated.

Following the structural analysis by XRD, Raman spectroscopy and PL measurements were employed to further probe local lattice distortions, defect-related states, and microstructural effects induced by the different heating protocols. Fig. 2 shows the Raman and PL spectra of the continuous ramp and isothermal insertion samples. In the Raman spectrum shown in Fig. 2 a, the CuO layer grown under the continuous ramp heating protocol exhibits three well-defined bands centered at 295, 345, and 631 cm^{-1}. For monoclinic CuO, group theory predicts a total of twelve vibrational modes at the Brillouin zone center of the primitive cell, described by the irreducible representation (4Au + 5Bu + Ag + 2Bg). Of these modes, six are infrared-active, three correspond to acoustic vibrations, and three are Raman-active (Ag + 2Bg). Previous Raman studies of monoclinic CuO report three Raman-active phonon modes located at approximately 297, 344, and 629 cm^{-1} at room temperature, corresponding to the Ag and Bg symmetries [19]. Experimentally, the Raman band observed at 295 cm^{-1} is attributed to the Ag mode, while the bands appearin at 345 and 631 cm^{-1} are associated with the Bg modes. The observed positions are close to the values reported in the literature, with slight deviations that may be associated with microstructural effects commonly observed in thermally grown CuO layers. The presence of these characteristic Raman bands confirms the formation of monoclinic CuO as the dominant phase in the analyzed region. In the Raman spectrum of the CuO layer grown under the isothermal insertion heating protocol (Fig. 2 d), three well-defined vibrational modes are observed at approximately 299, 346, and 629 cm^{-1}. The observed peak positions are also in good agreement with previously reported Raman data for bulk and polycrystalline CuO, confirming the formation of the tenorite phase in the sample obtained by isothermal insertion. The presence of sharp and well-defined Raman bands indicates a good degree of local structural order in the CuO layer. A closer inspection of the Raman spectra reveals that the peak positions for both heating protocols are nearly identical, with differences below 1.5 cm^{-1} for all observed modes, indicating a similar local bonding environment in the CuO layers. The full width at half maximum (FWHM) values show slightly broader Raman bands for the isothermal insertion sample compared to the continuous ramp sample (Table 2).

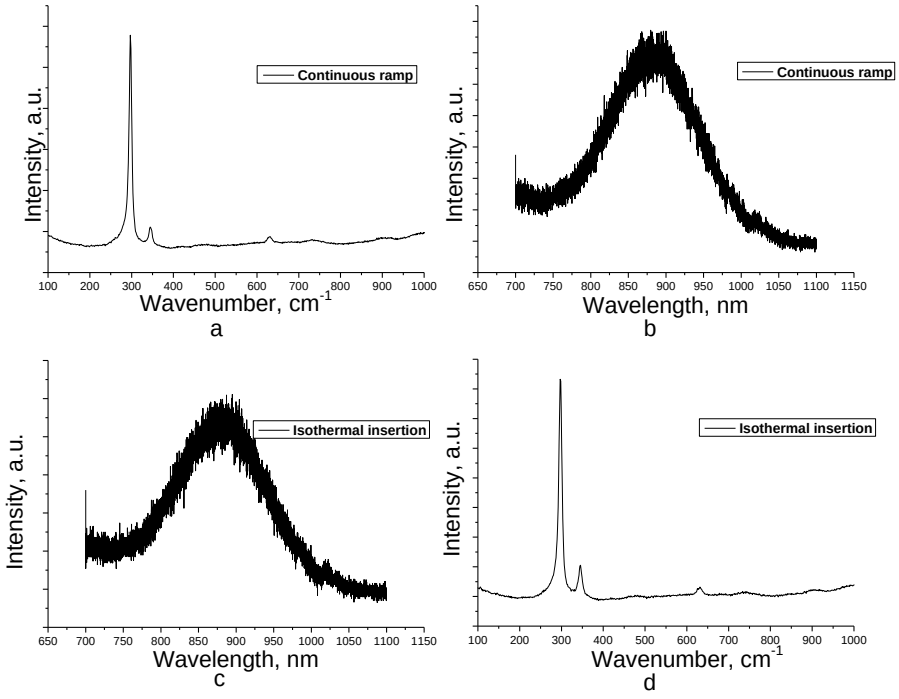

Fig. 2. Raman and photoluminescence, PL, spectra of CuO layers grown under different heating protocols: a, b – Raman and PL spectra for the continuous ramp protocol; c, d – PL and Raman spectra for the isothermal insertion protocol.

Table 2. Raman and photoluminescence peak positions and FWHM of CuO layers grown under continuous ramp and isothermal insertion heating protocols

Heating protocol	Raman peaks, cm^1	FWHM	PL peak, nm	FWHM
Continuous ramp	295	7.789	880	154
	345	9.0615		
	631	12.764		
Isothermal insertion	299	9.361	887	153
	346	10.021		
	629	13.746		

This modest increase in the FWHM suggests a somewhat higher degree of local lattice distortion or strain, in good agreement with the microstrain values derived from XRD analysis. Despite these minor differences, the overall Raman response confirms that the local structural characteristics of CuO remain largely preserved under both heating protocols. Fig. 2 b and c show the photoluminescence (PL) spectra of the CuO layers obtained under 633 nm excitation for the samples processed using the continuous ramp and isothermal insertion protocols, respectively. The sample processed under the continuous ramp protocol (Fig. 2 b) exhibits an emission maximum centered at 880 nm with a FWHM of 154 nm (Table 2), whereas the isothermal insertion sample (Fig. 2 c) shows a slight red shift, with the emission maximum located at 887 nm and a very similar FWHM of 153 nm. The large FWHM values, close to 150 nm, are consistent with PL dominated by defect-related recombination mechanisms, as broad emission bands are commonly associated with radiative transitions involving localized states in semiconducting oxides. In particular, near-infrared photoluminescence in CuO has been attributed to recombination processes involving oxygen vacancies, where electrons bound to donor-like defect states recombine with free or weakly bound holes, giving rise to emission bands in the 850 – 870 nm range [20].Despite these slight differences, the overall spectral shape remains essentially unchanged, indicating that the thermal protocol does not introduce additional radiative pathways but rather slightly modulates the energetic distribution of existing defect states. This behavior is consistent with the Raman analysis discussed above, where changes in peak widths and spectral definition were also associated with microstructural effects rather than with phase transformations.

The electrical properties of the CuO layers grown under the two heating protocols were evaluated by Hall effect measurements at room temperature. Both samples exhibited p-type conductivity, as indicated by the positive sign of the Hall coefficient, which is consistent with the intrinsic defect chemistry of CuO, where copper vacancies and oxygen-related defects act as acceptor states [21]. Table 3 summarizes the hole concentration (p), Hall mobility (μ_h), and electrical conductivity (σ) obtained for the samples processed using the isothermal insertion and continuous ramp protocols. For the isothermal insertion protocol, a hole concentration of 7.188×10^{15} cm^{-3} was obtained, along with a Hall mobility of 48.26 $cm^2\ V^{-1}\ s^{-1}$, resulting in an electrical conductivity on the order of 5.557×10^{-2} $(\Omega\ cm)^{-1}$. Similar values were obtained for the continuous ramp protocol, with the electrical parameters remaining within the same order of magnitude. Despite the marked differences observed in crystallographic texture and microstructural parameters between the two heating protocols, as revealed by XRD analysis, the electrical transport properties show only minor variations. In particular, the strong preferential orientation along the (−202) plane observed for the sample obtained in the continuous ramp protocol (characterized by a texture coefficient of 4.17), does not lead to a significant enhancement or degradation of carrier concentration or mobility when compared to the isothermal insertion sample, which exhibits a more distributed texture across multiple crystallographic planes. This behavior suggests that, under the present oxidation conditions, charge transport in thermally grown CuO layers is governed primarily by intrinsic point defects rather than by crystallographic texture or grain orientation effects. Although the continuous ramp protocol results in larger crystallite size and reduced microstrain and dislocation density, these improvements in crystalline quality do not translate into a substantial modification of the macroscopic electrical properties. Furthermore, the presence of a weak Cu_2O phase in the XRD diffractogram of continuous ramp sample does not appear to significantly affect charge transport, likely due to its low volume fraction. Overall, the Hall effect results indicate that while the heating protocol plays a decisive role in controlling the microstructural characteristics and crystallographic texture of CuO layers, its influence on room-temperature electrical transport properties is comparatively limited. This decoupling between texture evolution and electrical behavior highlights the robustness of the p-type conduction mechanism in thermally oxidized CuO under the conditions investigated.

4. CONCLUSIONS

CuO layers were obtained by thermal oxidation of Cu sheets at 900 °C using isothermal insertion and continuous ramp heating protocols. XRD analysis demonstrates that the heating protocol strongly affects the crystallographic texture of the resulting CuO layers.

Table 3. Electrical properties of CuO layers determined by Hall effect measurements

Heating protocol	Hole concentration, cm^{-3}	Hall mobility, $cm^2/V{\cdot}s$	Electrical conductivity, $\Omega^{-1}{\cdot}cm^{-1}$
Isothermal insertion	7.188×10^{15}	48.26	5.557×10^{-2}
Continuous ramp	7.973×10^{15}	41.04	5.242×10^{-2}

The isothermal insertion protocol yields a distributed preferential orientation, whereas the continuous ramp protocol promotes a strong texture along the (−202) plane and enhanced grain growth, although traces of Cu_2O are also detected under gradual heating. Raman spectroscopy and photoluminescence measurements indicated that the differences induced by the heating protocol are mainly associated with microstructural features and defect-related states rather than phase transformations. Hall effect measurements confirm p-type conductivity for all samples, with similar electrical properties for both protocols, indicating that charge transport in thermally oxidized CuO is weakly affected by texture and defect-related variations. The heating protocol therefore provides an effective means to tailor crystallographic texture while preserving stable electrical behavior.

Acknowledgments

The authors thank to Ing. Francisco Rodríguez-Melgarejo from CINVESTAV-IPN unidad Queretaro, for its technical support in the Raman and photoluminescence measurements reported in this work.

REFERENCES

1. **Saleem S., Jabbar, A.H., Jameel, M.H., Rehman, A., Kareem, Z.H., Abbas, A.H., Ghaffar, Z., Razzaq, S.A., Pashameah, R.A., Alzahrani, E., Ng, E.P., Sapuan, S.M.** Enhancement in Structural, Morphological, and Optical Properties of Copper Oxide for Optoelectronic Device Applications *Nanotechnology Reviews* 11 (1) 2022: pp. 2827 – 2838. https://doi.org/10.1515/ntrev-2022-0473
2. **Prakash, A., Mishra, V., Mahesha, M.G.** Probing Intrinsic Defects of Aluminium-doped CuO Thin Films for Solar Cell Applications *RSC Advances* 14 2024: pp. 35184 – 35197. https://doi.org/10.1039/D4RA06413E
3. **De Carlo, I., Baudino, L., Klapetek, P., Serrapede, M., Michieletti, F., De Leo, N., Pirri, F., Boarino, L., Lamberti, A., Milano, G.** Electrical and Thermal Conductivities of Single CuxO Nanowires *Nanomaterials* 13 (21) 2023: pp. 2822. https://doi.org/10.3390/nano13212822
4. **Zhang, M., Lv, X., Wang, T., Pei, W., Yang, Y., Li, F., Yin, D., Yu, H., Dong, X.** CuO-based Gas Sensor Decorated by Polyoxometalates Electron Acceptors: From Constructing Heterostructure to Improved Sensitivity and Fast Response for Ethanol Detection *Sensors and Actuators B: Chemical* 415 2024: pp. 136016.
5. **Alabdan, H., Alwabsi, A., Alsagrey, A.M., AlKhulaif, F.H., Abdelgawad, M.E., AlQahtani, N.J., Al-Malki, A., Alfahad, A., Alrubaian, W.S., Alsahl, F.M., Mallick, T.K.** Usage of CuO in Dye-Sensitized Solar Cells and CuO-Based Dyesensitized Solar Cells: A Review *IEEE Journal of Photovoltaics* 12 (6) 2022: pp. 1445 – 1452. https://doi.org/10.1109/JPHOTOV.2022.3196812
6. **Kaur, J., Khanna, A., Kumar, R., Chandra, R.** Growth and Characterization of Cu_2O and CuO Thin Films *Journal of Materials Science: Materials in Electronics* 33 2022: pp. 16154 – 16166. https://doi.org/10.1007/s10854-022-08506-0
7. **Parvathy, T., Muhammed Sabeer, N.A., Mohan, N., Pradyumnan, P.P.** Effect of Dopant Gas Pressure on the Growth of Magnetron Sputtered CuO Thin Films for Electrical and Optical Applications *Optical Materials* 125 2022: pp. 112031. https://doi.org/10.1016/j.optmat.2022.112031
8. **Wang, J., Russo, P.A., Pinna, N.** Impact of Surface Hydroxyl Groups on CuO film Growth by Atomic Layer Deposition *Langmuir* 39 (33) 2023: pp. 11603 – 11609. https://doi.org/10.1021/acs.langmuir.3c01109
9. **Kim, C.K., Drozdov, I.K., Fujita, K., Davis, J.C.S., Božović, I., Valla, T.** In-situ Angle-Resolved Photoemission Spectroscopy of Copper-Oxide Thin Films Synthesized by Molecular Beam Epitaxy *Journal of Electron Spectroscopy and Related Phenomena* 257 2022: pp. 146775. https://doi.org/10.1016/j.elspec.2018.07.003
10. **Jagadish, K.A., Kekuda, D.** Thermal Annealing Effect on Phase Evolution, Physical Properties of DC Sputtered Copper Oxide Thin Films and Transport Behavior of ITO/CuO/Al Schottky Diodes *Applied Physics A* 130 2024: pp. 315. https://doi.org/10.1007/s00339-024-07464-0
11. **Mahana, D., Mauraya, A.K., Singh, P., Muthusamy, S.K.** Evolution of CuO Thin Films Through Thermal Oxidation of Cu Films Prepared by Physical Vapour Deposition Techniques *Solid State Communications* 366 – 367 2023: pp. 115152. https://doi.org/10.1016/j.ssc.2023.115152
12. **Khalil, S., Ganguly, A., Mariotti, D., Chakrabarti, S.** Transformation Study and Characterization of Cu-BTC MOF-Derived Nanoporous Copper Oxide *Materials Horizons* 12 2025: pp. 862 – 876. https://doi.org/10.1039/D4MH01085J
13. **Mastache, J.M., López, R., Vigueras Santiago, E., Soriano Vargas, O.** Platinum (Pt), Gold (Au), and Silver (Ag) Ohmic Contacts to Cupric Oxide (CuO) Films Deposited by Air-based Sputtering and Thermal Annealing *Results in Physics* 46 2023: pp. 106292. https://doi.org/10.1016/j.rinp.2023.106292
14. **Massalski, T.B.** Structure of Metals: Crystallographic Methods, Principles, and Data. New York: McGraw-Hill; 1966.
15. **Cruz Almazán, M.A., Vigueras Santiago, E., López, R., Hernández López, S., Castrejón Sánchez, V.H., Esparza A, Encarnación Gómez C.** Cu_4O_3 Thin Films Deposited by Non-Reactive RF-Magnetron Sputtering from a Copper Oxide Target *Revista Mexicana de Fisica* 67 (3) 2021: pp. 495 – 499. https://doi.org/10.31349/revmexfis.67.495
16. **Košiček, M., Zavašnik, J., Baranov, O., Šetina Batič, B., Cvelbar, U.** Understanding the Growth of Copper Oxide Nanowires and Layers by Thermal Oxidation Over a Broad Temperature Range at Atmospheric Pressure *Crystal Growth and Design* 22 2022: pp. 6656 – 6666. https://doi.org/10.1021/acs.cgd.2c00863
17. **Wang, Y., Ghanbaja, J., Soldera, F., Migot, S., Boulet, P., Horwat, D., Mücklich, F., Pierson, J.F.** Tuning the Structure and Preferred Orientation in Reactively Sputtered Copper Oxide Thin Films *Applied Surface Science.* 335 2015: 85 – 91. https://doi.org/10.1016/j.apsusc.2015.02.028
18. **Ben Messaoud, O., Ouahab, A., Rahmane, S., Hettal, S., Kater, A., Sayad, M., Attouche, H., Gherraf, N.** Optoelectronic and Dielectric Properties of Tenorite CuO Thin Films Sprayed at Various Molar Concentrations *Periodica Polytechnica Chemical Engineering* 68 (1) 2024: pp. 93 – 105. https://doi.org/10.3311/PPch.22136
19. **Hagemann, H.R., Bill, H., Sadowski, W., Walker, E.,**

François, M. Raman Spectra of Single Crystal CuO *Solid State Communications* 73 (6) 1990: pp. 447 – 451. https://doi.org/10.1016/0038-1098(90)90048-G

20. **Siddiqui, H., Qureshi, M.S., Haque, F.Z.** pH-Dependent Single-Step Rapid Synthesis of CuO Nanoparticles and Their Optical Behavior *Optics and Spectroscopy* 123 (6) 2017: pp. 903 – 912. https://doi.org/10.1134/S0030400X17120013
21. **Živković, A., de Leeuw, N.H.** Exploring the Formation of Intrinsic p-type and n-type Defects in CuO *Physical Review Mater*ials 4 (7) 2020: pp. 074606. https://doi.org/10.1103/PhysRevMaterials.4.074606